Enhanced Atmospheric Turbulence Resiliency with Successive Interference Cancellation DSP in Mode Division Multiplexing Free-Space Optical Links

Yiming Li, Zhaozhong Chen, Zhouyi Hu, *Member, IEEE,* David M. Benton, Abdallah A. I. Ali, Mohammed Patel, Martin P. J. Lavery, and Andrew D. Ellis, *Fellow, Optica*

Abstract—We experimentally demonstrate the enhanced atmospheric turbulence resiliency in a 137.8 Gbit/s/mode mode-division multiplexing free-space optical communication link through the application of a successive interference cancellation digital signal processing algorithm. The turbulence resiliency is further enhanced through redundant receive channels in the mode-division multiplexing link. The proof of concept demonstration is performed using commercially available mode-selective photonic lanterns, a commercial transponder, and a spatial light modulator based turbulence emulator. In this link, 5 spatial modes with each mode carrying 34.46 GBaud dual-polarization quadrature phase shift keying signals are successfully transmitted with an average bit error rate lower than the hard-decision forward error correction limit. As a result, we achieved a record-high mode- and polarization-division multiplexing channel number of 10, a record-high line rate of 689.23 Gbit/s, and a record-high net spectral efficiency of 13.9 bit/s/Hz in emulated turbulent links in a mode-division multiplexing free-space optical system.

Index Terms—Mode division multiplexing (MDM), free-space optics (FSO), multiple-input multiple-output (MIMO), successive interference cancellation (SIC), turbulence.

I. INTRODUCTION

FREE space optical (FSO) communication is a promising wireless communication technique for a wide range of applications. FSO systems can provide a very high unlicensed bandwidth for data transmission at more than one hundred Gigabits per second [1], and can also provide extremely long transmission distance, inherent security, and robustness to electromagnetic interference [2], [3].

Mode-division multiplexing (MDM) can be used in FSO communication systems to increase the throughput or mitigate the impact of atmospheric turbulence [4], [5]. A popular basis for MDM is orbital angular momentum (OAM) modes, which can be decomposed into the rotational symmetric complete orthogonal Laguerre–Gaussian (LG) modal basis set [6]–[8].

To further increase the transmission capacity, it is preferable to employ a complete orthogonal mode set, such as LG modes [9], where orthogonality guarantees negligible crosstalk, and the rotational symmetry guarantees good compatibility with conventional optical lenses and fiber based delivery with relatively low modal crosstalk [10].

Atmospheric turbulence can significantly reduce the system performance by introducing scintillation, beam wandering, beam spreading, angle-of-arrival fluctuations, and phase fluctuations [11]. The performance degradation is even more pronounced in a MDM FSO system as it can introduce the inter-mode crosstalk [7], [12]–[14].

Adaptive optics (AO) may be used to mitigate atmospheric turbulence effects [8], [15], [16], and may be assisted by a coaxial Gaussian beam as reference for MDM FSO systems [8]. Recently, machine learning techniques have also been employed in AO systems to improve the system performance or reduce the hardware cost [17]–[19]. However, the AO systems can not fully compensate for the turbulence effects and residual inter-mode crosstalk remains [8], [15], requiring a tradeoff between control bandwidth and compensation errors [16].

Multiple-input multiple-output (MIMO) digital signal processing (DSP) is another approach to mitigate the negative effects of atmospheric turbulence in the MDM FSO systems [20], [21]. MIMO DSP shifts the complexity from the optical to the digital domain, enabling rapid feed-forward channel state information (CSI) extraction. Most reported MIMO algorithms in optical communications are based on a minimum mean square error (MMSE) MIMO equalizer [20]–[24]. This works well in few-mode fibre (FMF) channels where the channel matrix is almost unitary [22]–[24], but introduces significant performance degradation in fading channels [20], [21], [25], where non-unitary channel matrices exist due to (a) significant inter-mode interference and (b) power leakage to the higher order modes which can not be received [12], [20]. Therefore, advanced MIMO decoders should be considered to better mitigate the negative effects of turbulence-induced fading. Successive interference cancellation (SIC) decoders, which have been employed in radio frequency communication systems and outperforms the MMSE MIMO decoders [26]–[29], is a good candidate for the MDM FSO systems.

It is widely accepted in the radio frequency wireless MIMO communication systems that adding redundant receive channels can provide extra diversity gain, which is beneficial to the
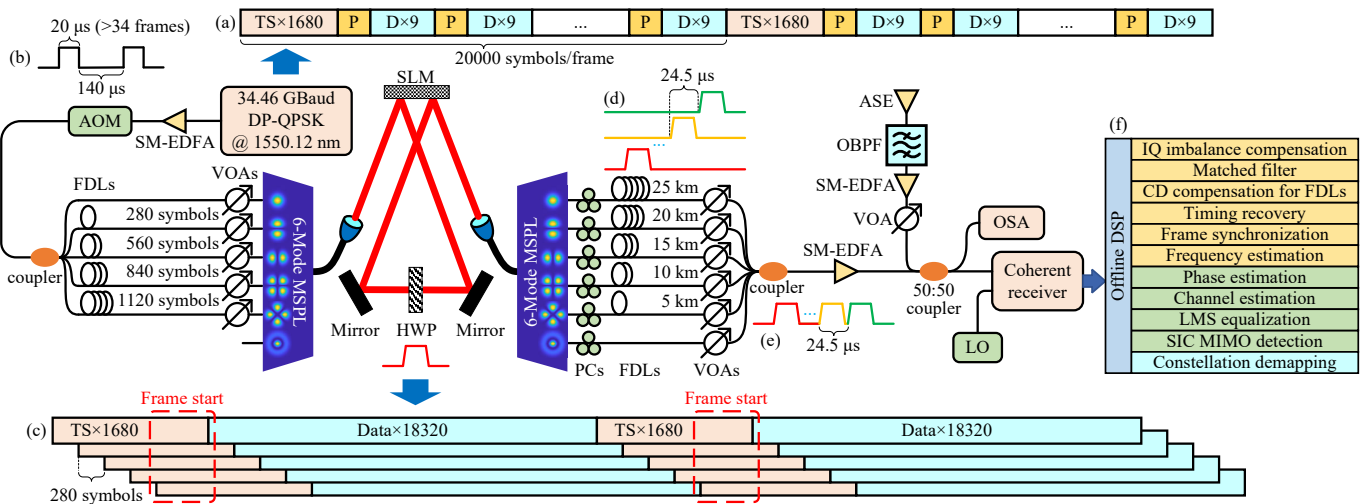
Fig. 1. The experimental setup. DP-QPSK: dual-polarization quadrature phase shift keying; TS: training sequence; P: pilot; D: data; SM-EDFA: single-mode erbium-doped fiber amplifier; AOM: acousto-optic modulator; FDLs: fibre delay lines; VOAs: variable optical attenuators; MSPL: mode-selective photonic lantern; SLM: spatial light modulator; HWP: half-wave plate; PCs: polarization controllers; ASE: amplified spontaneous emission; OBPF: optical bandpass filter; OSA: optical spectrum analyzer; DSP: digital signal processing; CD: chromatic dispersion; LMS: least mean squares; SIC: successive interference cancellation; MIMO: multiple-input multiple-output. (a) Frame structure generated by Ciena transponder; (b) signal burst after AOM; (c) delayed frame structure after transmitter FDLs; (d) time-division multiplexing (TDM) signal after receiver FDLs; (e) TDM signal after receiver coupler; (f) offline DSP.

bit error rate (BER) performance [25], [26]. In theoretical analysis, there are some researches on diversity gain for the MIMO FSO systems [30], [31]. However, in experimental MDM FSO systems, diversity gain has only been considered in special cases such as single-input multiple-output (SIMO) systems, or systems with multiple spatially separated apertures [5], [21]. To date, the generalized MIMO algorithms with redundant receive channels have not been applied to the experimental MDM FSO systems to combat turbulence induced fading yet.

In this paper, we experimentally demonstrated enhanced atmospheric turbulence resiliency in MDM FSO communication systems. In particular: (1) We validate for the first time that SIC MIMO decoding provides enhanced turbulence resiliency; (2) We provide the first demonstration that a generalized MIMO algorithm with redundant receive channels provides enhanced turbulence resiliency by comparing different MIMO systems (e.g. 10×10, 10×12, and 6×6 to 6×12); (3) We employ commercial components, including mode selective photonic lanterns (MSPLs) and coherent transponders to demonstrate practical applicability. As a result, we have demonstrated a record high independent channel number of 10, line rate of 689.23 Gbit/s, and net spectral efficiency of 13.9 bit/s/Hz in emulated turbulent MDM FSO links.

The remainder of this paper is organized as follows: the experimental setup is given in Section II, Section III proposes the selection of phase screens for turbulence generation, Section IV proposes the SIC MIMO DSP with redundant receive channels for enhanced turbulence resiliency, Section V provides the experimental results, and Section VI summarizes the key advantages of the proposed MDM FSO system.

II. EXPERIMENTAL SETUP

The experimental setup is shown in Fig. 1. At the transmitter, a Ciena WaveLogic 3 transponder with a 39.385 GSa/s onboard arbitrary waveform generator (AWG) was used to generate the 34.46 GBaud dual-polarization quadrature phase shift keying (DP-QPSK) signals at 1550.12 nm. As shown in Fig. 1(a), the signals had a pilot-aided frame structure with a frame length of 20,000 symbols. Each frame had a training sequence of 1680 symbols, and a pilot symbol for every 9 data symbols in the payload. The training sequence and the pilots were generated by a random permutation of balanced QPSK symbols. The data symbols were generated from a PRBS-15 pseudo random binary sequence (PRBS). The generated signals were shaped by a root-raised cosine (RRC) filter with a roll-off factor of 0.1. The signals were then amplified by a single-mode erbium-doped fibre amplifier (SM-EDFA). In order to emulate the use of independent transmitters and receivers, at the transmitter, the resultant optical signal was passed through an acousto-optical modulator (AOM), which was operated at a period of 160 µs and a duty cycle of 12.5%, generating a 20 µs signal burst (Fig. 1(b), more than 34 frames). The signals were then split into 5 copies by a fibre coupler and then each copy was delayed by a variable fibre delay line (FDL) with lengths of 0, 280, 560, 840, and 1120 symbols, respectively to generate decorrelated signals for different modes (Fig. 1(c)), and the decorrelation length between adjacent modes is 1/6th of the training sequence length. The decorrelated signals were then connected to 5 variable optical attenuators (VOAs) to compensate for the mode-dependent loss at the transmitter side to guarantee that each transmitted mode contributed approximately the same power at the receiver side. The attenuated signals were finally connected to the five lowest order linearly polarized (LP) modes of a 6-mode MSPL for mode multiplexing and then coupled into free space using a collimator with a focal length of 18.4 mm and a lens diameter of $D = 8.4$ mm.

In the FSO channel, we employed a spatial light modulator (SLM) with 1920×1152 pixels to emulate indefinite number of independent turbulence realizations. The size of each pixel

is $9.2 \times 9.2\,\mu m^2$. In order to modulate the both polarization components of the signal, we passed the collimated light through the SLM twice (red paths in Fig. 1). Simulated phase screen were displayed on the left and right half of the SLM. The distance between the collimators and the SLM, the mirrors and the SLM, and the two mirrors were ~50 cm, ~50 cm, and ~20 cm, respectively. During the first pass, the horizontal polarization component was modulated by turbulence phase screen. A half-wave plate (HWP) located in-between the first and second pass swapped the horizontal and vertical components. And then the unaffected component in the first pass was modulated by the same turbulence phase screen during the second pass. The selection of phase screens for turbulence generation will be detailed in Section III.

At the receiver side, the free-space beam was coupled into a FMF by a second identical $D = 8.4$ mm diameter FSO coupler with a focal length of 18.4 mm. The received signals were then demultiplexed by a second 6-mode MSPL at the receiver side. 6 polarization controllers were connected to the output of the MSPL to balance the received power in different polarization states. Afterwards, the 6 signals were delayed by the 25 km, 20 km, 15 km, 10 km, 5 km, and 0 km FDLs to enable the time-division multiplexing (TDM) receiver [22], [23], which is also used in our previous experiments to detect all the received channels using a single receiver for the lab demonstration [32], [33]. As shown in Fig. 1(d), the FDLs generated an approximately 24.5 μs delay between adjacent modes, which was slightly longer than the signal burst. 6 VOAs were then connected to the output of the FDLs to compensate for the mode-dependent loss of the devices at the receiver side. The TDM signals were then coupled into one single-mode fibre (Fig. 1(e)) and amplified by another SM-EDFA. Afterwards, the variable optical noise was loaded by a combination of an amplified spontaneous emission source, an optical bandpass filter, a SM-EDFA, a VOA, and a 50:50 coupler. The average optical signal-to-noise ratio (OSNR) was then measured by an optical spectrum analyzer to enable OSNR scanning. The resultant signal was received by a standard coherent receiver with a 50 GSa/s sampling rate and 23 GHz bandwidth oscilloscope. Finally, the received digital traces were demodulated and decoded by the offline DSP (Fig. 1(f)).

III. TURBULENCE GENERATION

In this work, we emulated the beam propagation in a thin phase turbulent channel representing a weak atmospheric turbulence, using a single aberration inducing phase screen implemented with a SLM to emulate each instantiation of the turbulent channel. The screens used were generated by implementing a power spectrum inversion method, in which phase screens are randomly generated by performing a Fast Fourier Transform (FFT) of associated spatial frequency power spectrum. The power spectrum that is commonly used for atmospheric turbulence is the von Kármán spectrum [11], that

has Fourier series coefficients, $c_{n,m}$, in the form,

$$
\begin{aligned}
c_{n,m} = & w(n,m) \frac{\sqrt{0.023}}{L} \left(\frac{2}{r_0}\right)^{\frac{5}{6}} \left(f_{x_n}^2 + f_{y_m}^2 + \frac{1}{L_0^2}\right)^{-\frac{11}{12}} \\
& \times \left\{ \exp\left[-\left(f_{x_n}^2 + f_{y_m}^2\right)\left(\frac{2\pi l_0}{5.92}\right)^2\right] \right\}^{\frac{1}{2}},
\end{aligned}
$$

(1)

where $w(n,m)$ is the random array that obey complex circular Gaussian statistics with zero-mean and unit-variance. $L = 8.832$ mm is the length of the 960×960 pattern. r_0 is the Fried's parameter. The spatial frequency grid is determined by parameters $f_{x_n} = n/L$ and $f_{y_m} = m/L$. Further, this power spectrum is influenced by the physical channel parameters that determine the largest, L_0 to smallest, l_0 eddies sizes present in a turbulent channel.

Turbulence-induced phase $\phi(x,y)$ can be generated by considering discrete x- and y-directed spatial frequencies denoted as f_{x_n} and f_{y_m}, respectively. To accurately represent modes like tilt aberration, the sub-harmonic can be employed [34], [35]. A 3×3 grid of 2D arrays of spatial frequencies is used, where the frequency grid spacing for each value of p is $1/(3^p L)$, and the corresponding Fourier series coefficient is $c_{n,m,p}$. A specific phase screen, $\phi(x,y)$ can then be computed as a sum of $N_p + 1$ independent screens using the formula

$$
\begin{aligned}
\phi(x,y) = & \sum_{n=-\infty}^{+\infty} \sum_{m=-\infty}^{+\infty} c_{n,m} \exp\left[j2\pi\left(f_{x_n}x + f_{y_m}y\right)\right] \\
& + \sum_{p=1}^{N_p} \sum_{n=-1}^{1} \sum_{m=-1}^{1} c_{n,m,p} \exp\left[j2\pi\left(f_{x_n}x + f_{y_m}y\right)\right].
\end{aligned}
$$

(2)

Each computed screen provides an individual instance of turbulence and can vary in strength, where the full impact of a particular turbulence strength can only be realized by considering an appropriate number of instances over time. It is generally considered that turbulence is approximately frozen at a time base close to the coherence time, commonly called the Greenwood frequency of the atmosphere and can vary between 60 Hz to 1 kHz depending on the particular environment condition [35]. Therefore, if a channel measurement is performed suitably faster than this Greenwood frequency, which is the typical case for the channel estimation algorithm in the high-speed coherent optical communication systems, then one single instance of turbulence needs to be considered when the channel mitigation strategies are applied.

In this paper, we considered two sets of 120 independent patterns, both with $L_0 = 10$ m and $l_0 = 0.1$ mm, for stronger ($r_0 = 0.8$ mm, $D/r_0 = 10.5$) and weaker ($r_0 = 3.0$ mm, $D/r_0 = 2.8$) turbulence, respectively. Example patterns are shown in Fig. 2(a) and Fig. 2(c), whilst Fig. 2(b) and Fig. 2(d) show the probability density function (PDF) of the normalized power in all modes at the receiver. The power is measured at the output of the receiver FMF, and the normalization process guarantees the average power to be 1, eliminating the influence of attenuation in the system. According to Fig. 2(b) and Fig. 2(d), the measured results agree well with normalized lognormal curve fits corresponding to scintillation indexes
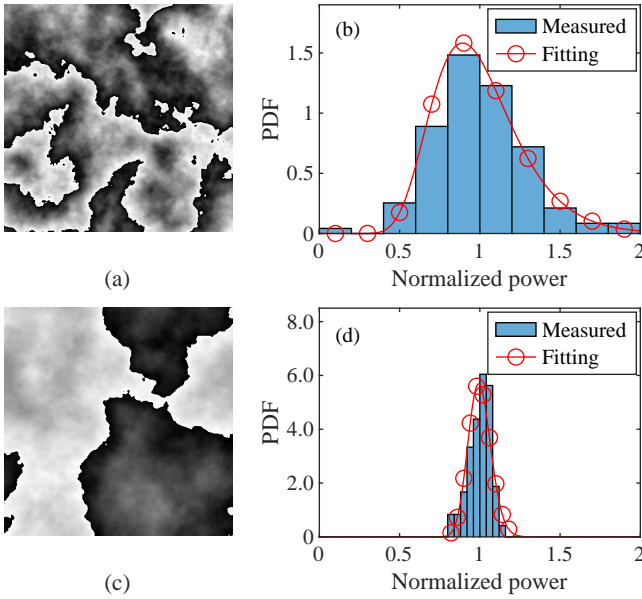
Fig. 2. The typical turbulence realizations ($L_0 = 10\,\mathrm{m}$, $l_0 = 0.1\,\mathrm{mm}$). PDF: probability density function. (a) The typical pattern of the stronger turbulence ($r_0 = 0.8\,\mathrm{mm}$); (b) The power distribution of the stronger turbulence ($\sigma_I^2 = 0.079$); (c) The typical pattern of the weaker turbulence ($r_0 = 3.0\,\mathrm{mm}$); (d) The power distribution of the weaker turbulence ($\sigma_I^2 = 0.0050$).
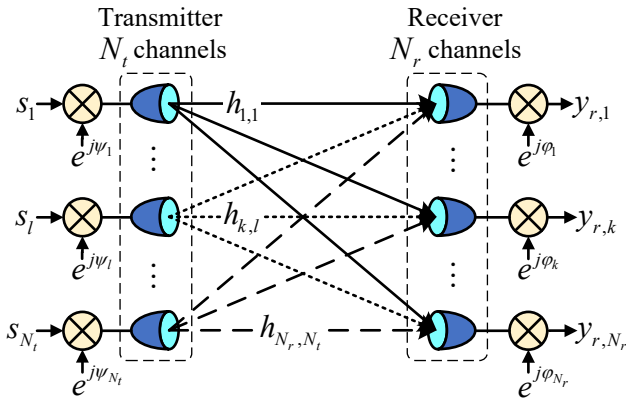

Fig. 3. Schematic diagram for MDM optical communication systems.

(σ_I^2) of 0.079 and 0.0050, respectively [11]. We believe the scintillation effect comes mainly from the scattering and inter-mode crosstalk due to the random phase distortion, and the power leakage to higher-order modes can not be coupled into the FMF due to its limited supported modes.

IV. MIMO DSP ALGORITHM

A. Preliminaries

As shown in Fig. 3, a generalized mathematical model for the TDM MDM optical communication system with N_t transmit channels and N_r receive channels can be given as

$$\mathbf{y}_r = \mathbf{\Phi} \mathbf{H} \mathbf{\Psi} \mathbf{s} + \mathbf{n}_r, \qquad (3)$$

where $\mathbf{y}_r$ is the $N_r \times 1$ received signal vector, $\mathbf{H}$ is the $N_r \times N_t$ channel matrix, $\mathbf{s}$ is the $N_t \times 1$ transmitted signal vector, $\mathbf{n}_r$ is the $N_r \times 1$ independent and identically distributed (i.i.d.) circularly-symmetric complex additive white

Gaussian noise (AWGN) vector, where the expectation and the variance of each element are 0 and N_0, respectively. $\mathbf{\Psi} = \mathrm{diag}\left(e^{j\psi_1}, \cdots, e^{j\psi_{N_t}}\right)$ and $\mathbf{\Phi} = \mathrm{diag}\left(e^{j\varphi_1}, \cdots, e^{j\varphi_{N_r}}\right)$ are the diagonal phase matrices of the transmit and receive channels, where ψ_l and φ_k are the phase noise at the lth transmit channel and the kth receive channel, respectively.

If the diagonal elements of $\mathbf{\Phi}$ and $\mathbf{\Psi}$ are approximately identical, corresponding to a single transmit laser and a local oscillator, both with phase matched fiber paths, then MIMO equalization may be carried out prior to phase estimation [22]. However, the approximately identical phase should be conserved by carefully splitting and delaying the LO beam or using multiple oscilloscopes at the receiver [23]. This extra complexity can be reduced by employing carrier-asynchronous algorithms to combat decorrelated LOs, but prior attempts have suffered from iterative phase and channel estimation structure [24]. Moreover, inherent difficulties exist in the above mentioned DSPs when employing advanced MIMO decoding algorithms such as SIC.

To accommodate these practical realities, we propose a new carrier-asynchronous DSP structure, which is shown in Fig. 1(f) (green text), to separate the MIMO decoder from the phase estimation, the channel estimation, and the ISI equalization. By doing so, redundant receive channels and advanced MIMO decoding algorithms such as SIC can be supported.

The phase and channel estimation algorithm is fully detailed in one of our previous work [36]. Noting the fact that the phases are well conserved at the transmitter side, we can set $\mathbf{\Psi}$ to a $N_t \times N_t$ identity matrix as reference. Therefore, (3) can be simplified to

$$\mathbf{y}_r = \mathbf{\Phi} \mathbf{H} \mathbf{s} + \mathbf{n}_r. \qquad (4)$$

After the phase and channel estimation, we can obtain $\hat{\mathbf{\Phi}}$ and $\hat{\mathbf{H}}$, which are the estimations of $\mathbf{\Phi}$ and $\mathbf{H}$, respectively. And the phase information can be cancelled out as

$$\mathbf{y} = \hat{\mathbf{\Phi}}^H \mathbf{y}_r \approx \mathbf{H}\mathbf{s} + \hat{\mathbf{\Phi}}^H \mathbf{n}_r = \mathbf{H}\mathbf{s} + \mathbf{n}, \qquad (5)$$

where $(\cdot)^H$ is the Hermitian adjoint operator and $\mathbf{n} = \hat{\mathbf{\Phi}}^H \mathbf{n}_r$. Moreover, $\mathbf{n}$ has the same statistical property as $\mathbf{n}_r$.

Afterwards, a MIMO equalizer should be introduced to mitigate the negative influence from ISI. We only update the coefficients at the known pilot symbols $\mathbf{s}_p$ in the least mean squares (LMS) equalizer. The error signal of the LMS equalizer is $\varepsilon = \mathbf{I}_{eq} - \hat{\mathbf{I}}_{eq}$, where the desired output of the equalizer is $\mathbf{I}_{eq}$, and the actual output of the equalizer is $\hat{\mathbf{I}}_{eq}$. Moreover, we modified the desired output of our MIMO equalizer to

$$\mathbf{I}_{eq} = \hat{\mathbf{H}}\mathbf{s}_p, \qquad (6)$$

which is different from $\mathbf{I}_{eq} = \mathbf{s}_p$ in the conventional MIMO equalizers [37]. By doing so, the ISI can be mitigated without decoding the symbols, and an arbitrary MIMO decoding algorithm, such as SIC, can be applied after the MIMO equalization.
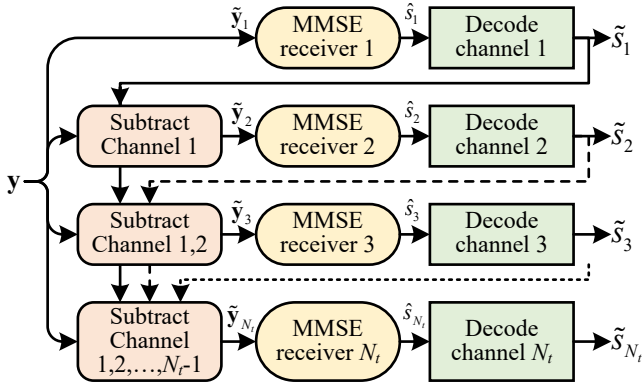
Fig. 4. Schematic diagram for the SIC algorithm.

B. Successive Interference Cancellation

To focus on the kth transmit channel, we can rewrite (5) as

$$\mathbf{y} = \mathbf{H}\mathbf{s} + \mathbf{n} = \sum_{i=1}^{N_t} \mathbf{h}_i s_i + \mathbf{n} = \mathbf{h}_k s_k + \sum_{\substack{i=1 \\ i \neq k}}^{N_t} \mathbf{h}_i s_i + \mathbf{n}, \quad (7)$$

where $\mathbf{h}_i$ is the ith column vector of the channel matrix $\mathbf{H}$, and s_i is the ith element of the transmitted signal vector $\mathbf{s}$. For the kth channel, the second term in the last equation is referred to as the inter-channel interference (ICI). We may notice that the ICI can be reduced if we can properly cancel out some of the interfering channels.

The schematic diagram for the SIC algorithm is shown in Fig. 4. The strategy of the SIC algorithm is to successively cancel out the interference of channels which have already been decoded [26]. For the kth channel, the subtraction process can be written as

$$\tilde{\mathbf{y}}_k = \mathbf{y} - \sum_{i=1}^{k-1} \hat{\mathbf{h}}_i \tilde{s}_i, \quad (8)$$

where $\hat{\mathbf{h}}_i$ is the ith column vector of the estimated channel matrix $\hat{\mathbf{H}}$, and $\tilde{s}_i$ is the decoded symbol in the ith channel. If the channel matrix is accurately estimated and the first $k-1$ symbols are properly decoded, (8) can be rewritten as

$$\tilde{\mathbf{y}}_k \approx \mathbf{h}_k s_k + \sum_{i=k+1}^{N_t} \mathbf{h}_i s_i + \mathbf{n}, \quad (9)$$

where the approximation indicates that the nonlinear error propagation may occur in this process if estimation or decoding error occurs [26]. However, the impact of this phenomenon can be minimized by using an optimal decoding order for each frame of the signal [28]. Moreover, it will be shown in Section V that we can still achieve a significantly better decoding performance by using the SIC algorithm.

After the subtraction process, the first $k-1$ channels are cancelled out. Therefore, the kth MMSE receiver should be modified to

$$\hat{s}_k = \left[\left(\hat{\mathbf{H}}_k \hat{\mathbf{H}}_k^H + N_0 \mathbf{I}_{N_r \times N_r} \right)^{-1} \hat{\mathbf{h}}_k \right]^H \mathbf{y}_k, \quad (10)$$

where $\hat{\mathbf{H}}_k = \left[\hat{\mathbf{h}}_k, \hat{\mathbf{h}}_{k+1}, \cdots, \hat{\mathbf{h}}_{N_t} \right]$, and $\mathbf{I}_{N_r \times N_r}$ represents the $N_r \times N_r$ identity matrix.

Finally, decoding in the kth channel can be calculated using the conventional decision rule as [25]

$$\tilde{s}_k = \arg \min_{\tilde{s}_k \in \mathcal{S}} \left(|\tilde{s}_k - \hat{s}_k| \right), \quad (11)$$

where $\mathcal{S}$ represents the set of all possible transmitted symbols, and $|\cdot|$ is the modulus operator for complex numbers.

C. Vector Space Explanation

In order to better understand why the proposed MIMO DSP algorithm can obtain enhanced atmospheric turbulence resiliency, Fig. 5 gives an vector space explanation for a system with 3 receive channels. In order to simplify the analysis, we only consider the special situation of negligible AWGN, where the MMSE algorithm degenerates to multiplying by a Moore–Penrose inverse matrix of $\mathbf{H}$, which can also be regarded as a projection and a scaling of the column vectors in $\mathbf{H}$. The AWGN in a practical system should be considered as another dimension in the random vector space and analogous analysis can then apply to the generalized situation with AWGN.

Fig. 5(a) illustrates a 3×3 linear MMSE MIMO decoder in vector space. Considering the fact that the scaling effect is just for normalization, we are only interested in the projection effect. For arbitrary $\mathbf{h}_k$, the effective projection $\tilde{\mathbf{h}}_k$ should be in the 1 dimensional orthogonal complement of the subspace spanned by $\{\mathbf{h}_i | 1 \leqslant i \leqslant N_t, i \neq k\}$ to eliminate the negative influence of ICI.

Fig. 5(b) illustrates a 3×3 SIC MIMO decoder. In the first channel, no interference cancellation is performed and the same performance as the MMSE decoder should be expected. However, when decoding the second channel, the first channel can be cancelled out, and $\tilde{\mathbf{h}}_2$ is a projection in the orthogonal complement of $\mathbf{h}_3$, which is a 2 dimensional vector subspace. Therefore, the degree of freedom is increased to 2 for the second channel. Similarly, the last channel needs no projection and all the 3 degrees of freedom can be exploited. As a result, the effective projections in the SIC system will be longer than or equal to the effective projections in the MMSE system, and a larger effective signal-to-interference-plus-noise ratio (SINR) can be achieved in the SIC system.

Fig. 5(c) illustrates a 2×3 MMSE MIMO decoder which has redundant receive channels. The third channel is directly cancelled out because we are not transmitting any symbols in that channel. As a result, arbitrary $\mathbf{h}_k$ can always be projected onto a 2 dimensional orthogonal complement subspace and a better turbulence resiliency can be obtained.

As a proof-of-concept illustration, Fig. 6 depicts the BER curves of each channel in the simulated SIC and MMSE MIMO systems. Here we use a channel matrix,

$$\mathbf{H} = \begin{bmatrix} -0.87 - 0.64j & 0.12 + 0.88j & 0.50 + 0.73j \\ -1.18 + 0.61j & -0.53 - 0.45j & -0.25 + 0.31j \\ -0.24 + 0.36j & -0.84 - 0.32j & 0.26 + 0.18j \end{bmatrix}, \quad (12)$$

for the 3×3 systems, and the first two columns of (12) for the 2×3 MMSE system. In the 3×3 SIC system, the first decoded
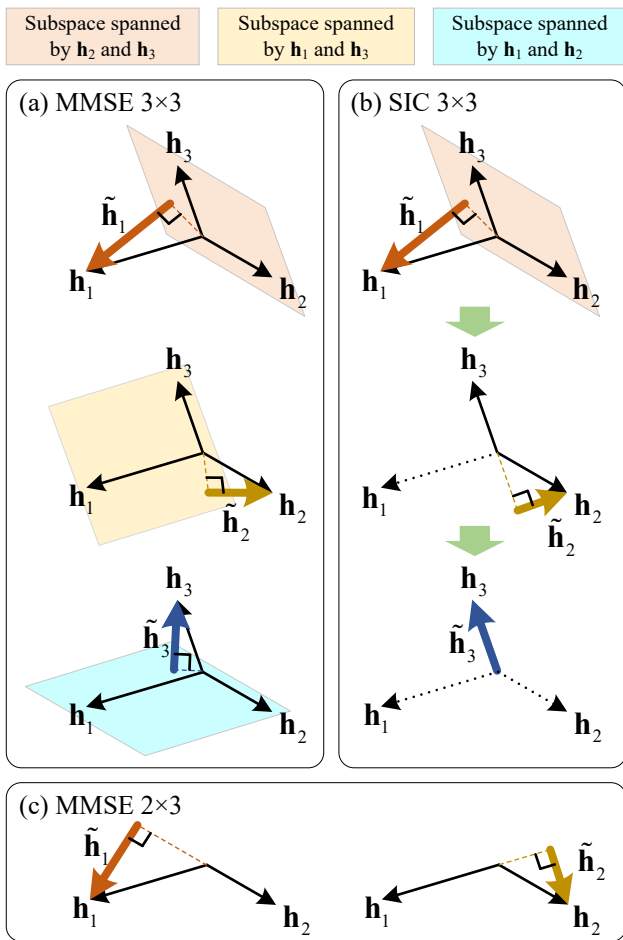
Fig. 5. The vector space explanation for the enhanced atmospheric turbulence resiliency. $\mathbf{h}_k$ is the kth column vector in the channel matrix $\mathbf{H}$, and $\tilde{\mathbf{h}}_k$ is the effective projection of $\mathbf{h}_k$. The vectors cancelled out by the SIC are represented by dotted vectors. (a) the 3×3 MMSE MIMO decoder; (b) the 3×3 SIC MIMO decoder; (c) the 2×3 MMSE MIMO decoder with redundant receive channels.

Fig. 6. BER curves of each channel in the simulated SIC and MMSE MIMO systems. Ch: channel.

TABLE I
EXPERIMENTAL PARAMETERS

Parameter	Value
Wavelength	1550.12 nm
Laser linewidth	100 kHz
Symbol format	DP-QPSK
Baud rate	34.46 GBaud
Roll-off factor	0.1
Receiver sampling rate	50 GSa/s
Hard-decision forward error correction (HD-FEC) limit with 6.25% overhead [38]	4.7×10^{-3}
Diameter of the receiver lens (D)	8.4 mm
Fried's parameter (r_0) for weaker turbulence	3.0 mm
Fried's parameter (r_0) for stronger turbulence	0.8 mm
Inner scale of turbulence (l_0)	0.1 mm
Outer scale of turbulence (L_0)	10 m

channel has the same performance as the 3×3 MMSE system, as they use the same MMSE receiver. However, the second and the third channel outperforms the 3×3 MMSE system because of the interference cancellation process, which offers extra degrees of freedom. On the other hand, both the channels in the 2×3 MMSE system outperforms the corresponding channels in the 3×3 MMSE system, indicating an extra degree of freedom provided by the redundant receive channel.

It is also worth noting that employing the SIC algorithm or adding redundant receive channels can only improve the performance in the non-orthogonal channels (e.g. turbulent channels). In an ideal channel with mutually orthogonal column vectors in the channel matrix (e.g. the orthogonality can be well conserved in short FMF link or back-to-back FSO link without turbulence), the equation $\tilde{\mathbf{h}}_k = \mathbf{h}_k$ holds. Therefore, the optimal system performance can be achieved by simply employing the conventional MMSE MIMO decoder.

V. EXPERIMENTAL RESULTS

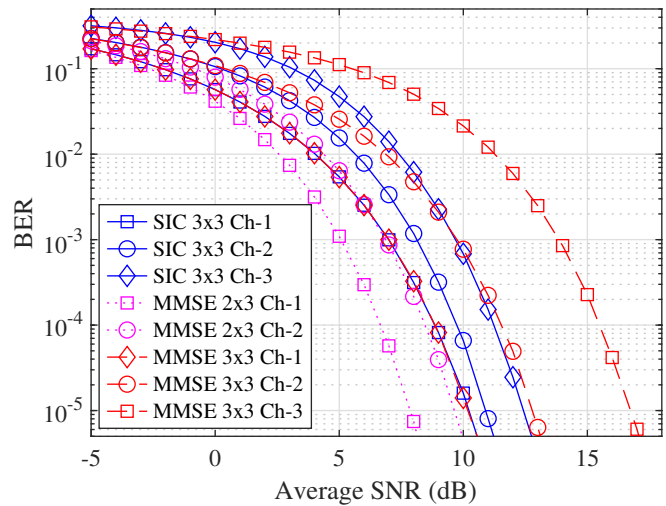Table I lists the experimental parameters for our MDM FSO communication system.

First, we experimentally examine the BER performance against average OSNR of the 10×12 MIMO system under different turbulence conditions, which is shown in Fig. 7. The theoretical reference curve assumes that: (1) The channel matrix is a $N_r \times N_t$ submatrix of a $N_r \times N_r$ unitary matrix; (2) No other imperfection except the AWGN exists. For the turbulence free situation, a blank pattern with factory pre-calibration is used in the system, here observe a ~2.2 dB implementation penalty for the SIC system at the hard-decision forward error correction (HD-FEC) limit, which we believe is dominated by the inter-mode crosstalk and residual mode-dependent losses in the MSPL pair. As expected, these imperfections have a slightly higher impact on the MMSE system (~2.7 dB implementation penalty). In the weaker turbulence case, the SIC system has a ~3 dB penalty but the penalty for the MMSE system is ~4.2 dB, which indicates a moderate reduction in channel matrix orthogonality. For the stronger turbulence, a larger penalty of ~6.9 dB is observed in the SIC system, but the MMSE system does not even achieve the HD-
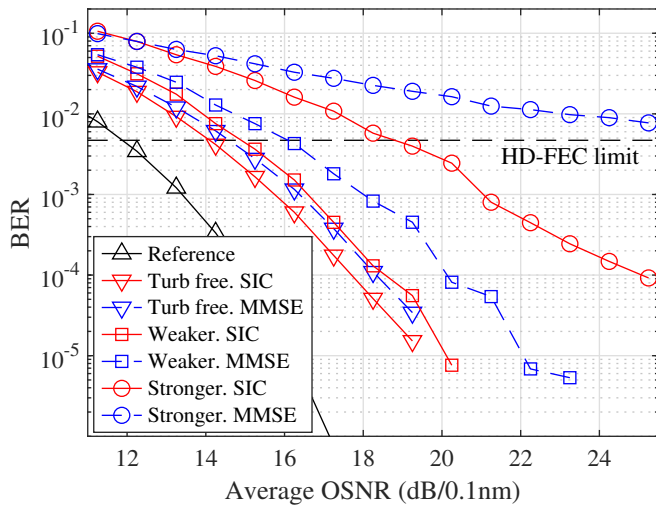
Fig. 7. Average BER curves of the 10×12 MIMO system under different turbulence intensities. Reference: Theoretical reference curve in an ideal system; Turb free: turbulence free system with a blank pattern. Weaker: typical weaker turbulence pattern when $r_0 = 3.0$ mm; Stronger: typical stronger turbulence pattern when $r_0 = 0.8$ mm.
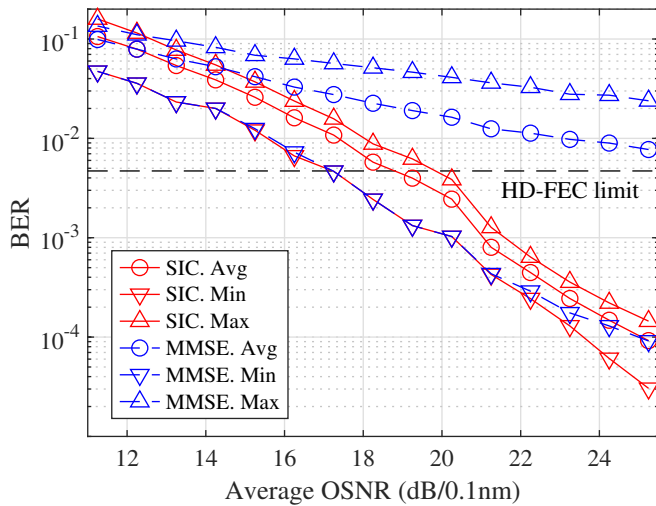

Fig. 8. BER curves of the 10×12 SIC (red lines) and MMSE (blue dotted lines) MIMO systems under the stronger turbulence when $r_0 = 0.8$ mm. Avg (circles): average BER; Min (lower triangles): the best channel with minimum BER at each average OSNR; Max (upper triangles): the worst channel with maximum BER at each average OSNR.

FEC limit, and the loss of channel matrix orthogonality is severe. The result in the stronger turbulence case also indicates that the proposed DSP algorithm has only mitigated rather than eliminated the negative influence of atmospheric turbulence.

In order to better understand the enhanced turbulence resiliency by the proposed SIC system, Fig. 8 depicts the BER of the best channel (the channel with minimum BER at each average OSNR), the worst channel (the channel with maximum BER at each average OSNR), and the average BER of all channels (also shown in Fig. 7) in the stronger turbulence. The best channels in both the SIC system and the MMSE system have similar BER performance, this is because we don't execute any interference cancellation for the first decoded channel in the SIC system. At the high OSNR region,

the best channel in the SIC system performs slightly better than the MMSE system. This is because the second decoded channel may obtain a better BER performance by cancelling out the first decoded channel. On the other hand, the worst channel in the SIC system has a much better performance than it in the MMSE system. This is because a higher effective SINR can be achieved in the SIC system by cancelling out the previously decoded channels. Considering the fact that the worst channel is the dominant factor in the average BER performance, the SIC system can obtain a significantly lower average BER in turbulent channels.

The constellation diagrams for the 10×10 and 10×12 MIMO systems under the stronger turbulence case are depicted in Fig. 9 without noise loading. The SIC order is given at the bottom left of each constellation. Because the channel matrices are different between the 10×10 and 10×12 MIMO systems, the SIC order may also be different. As shown in Fig. 9, the 10×10 and 10×12 SIC systems have a significantly lower error vector magnitude (EVM) than the 10×10 and 10×12 MMSE systems, respectively. This is because certain ICI is cancelled out by applying the SIC algorithm. However, no ICI is cancelled out in the first decoded channel (LP_{21bY} in both cases). In this channel, identical EVM performance is observed in both SIC and MMSE decoders. On the other hand, a comparison between the 10×10 and 10×12 MMSE MIMO systems shows that 1 more redundant receive mode (2 more redundant receive channels) can significantly reduce the EVM of the constellation in all the 10 channels. Compared with the 10×10 SIC MIMO system, We can also obtain a better average EVM performance in the 10×12 SIC MIMO system because of the information obtained from the 2 redundant receive channels (EVM = 21.23% for the 10×12 SIC MIMO system and EVM = 25.78% for the 10×10 SIC MIMO system, respectively), although a higher EVM in specific channels (e.g. LP_{21aY}) may be observed due to the different SIC order. Moreover, less nonlinear propagation (apparently discrete points in the diagram, see for example LP_{01X}) is also observed in the 10×12 SIC MIMO system. This is also because of the information obtained from the 2 redundant receive channels and less symbol error occurs in the decoded channels.

We tested 120 independent turbulence patterns under the stronger turbulence case without noise loading. As shown in Fig. 10, the BER of the SIC system is consistently lower than the MMSE system. As a result, the average BER among different turbulence realizations is decreased by an order of magnitude, from 8.02×10^{-3} in the MMSE system to 4.76×10^{-4} in the SIC system (well below the HD-FEC limit). The probability distribution of the BER in Fig. 10 is depicted in Fig. 11 for better clarity. Because of the limited length of our recorded data, the BER is taken as being below 10^{-6} for the 18 turbulence realizations where no errors we recorded. If we consider an outage when the BER is larger than the HD-FEC limit, we have an outage probability of 48.3% in the MMSE system and only 2.5% in the SIC system, suggesting a more robust transmission using SIC.

To further illustrate the enhanced turbulence resiliency obtained from the redundant receive channels, we increased
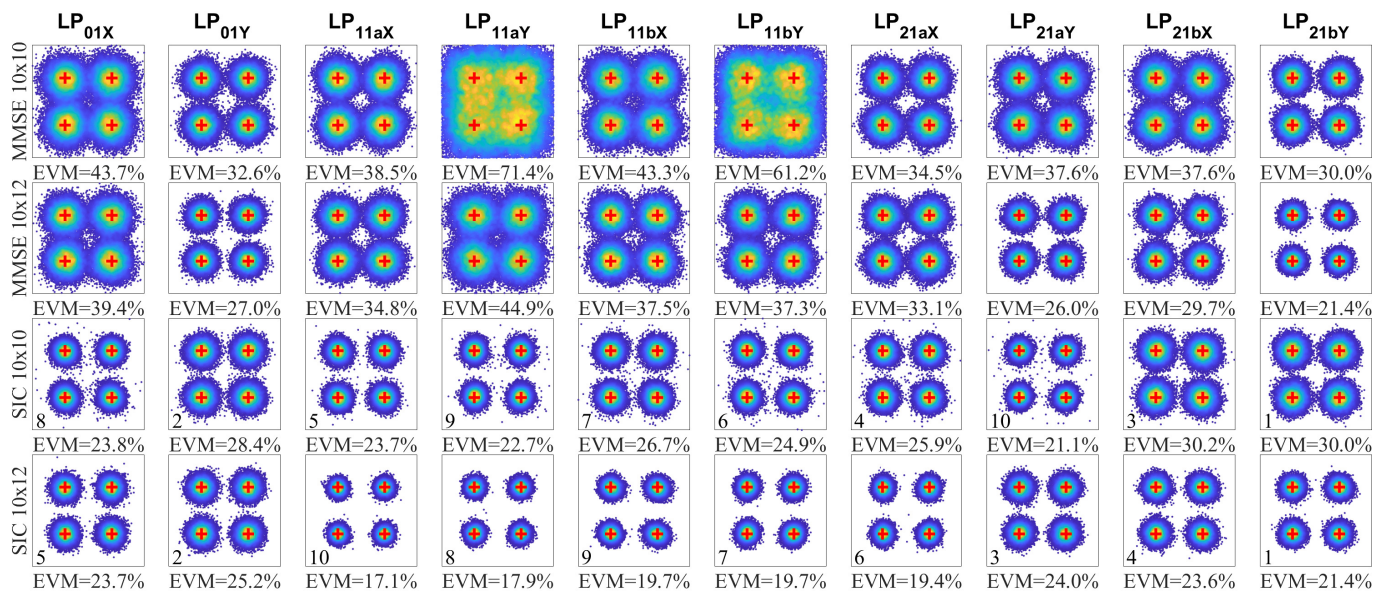
Fig. 9. Constellation diagrams of different transmitted channels for the 10×10 MMSE (the first row), 10×12 MMSE (the second row), 10×10 SIC (the third row), and 10×12 SIC (the last row) MIMO configurations without noise loading. The SIC order is given at the bottom left of each constellation. EVM: error vector magnitude. Red crosses: reference QPSK constellation points.
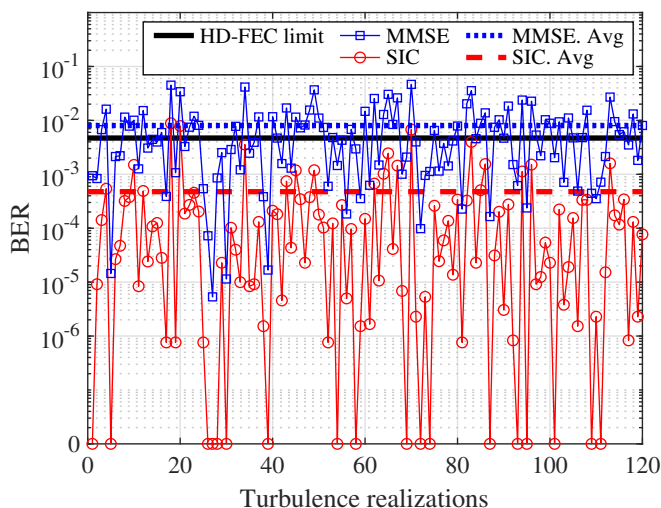

Fig. 10. The BER performance of the 10×12 MIMO system under 120 stronger turbulence realizations.

Fig. 11. The probability distribution of the BER performance in the 10×12 system under 120 stronger turbulence realizations.

the ratio of received to transmitted channels by disabling the two highest order mode inputs of the transmitter. Fig. 12 depicts the BER performance against average OSNR of a 6×12 MIMO system under the same turbulence conditions as Fig. 7. For the turbulence free situation, a blank SLM pattern with factory pre-calibration is used in the system. In this turbulence free scenario, we observe a ~1.4 dB implementation penalty between the reference and the SIC system at the HD-FEC limit, while the MMSE system has a slightly higher implementation penalty of ~1.5 dB. In the weaker turbulence case, the performance of the SIC system has a ~1.7 dB implementation penalty, compared to ~2.0 dB for the MMSE system. In the stronger turbulence case, a larger implementation penalty of ~4.0 dB is observed in the
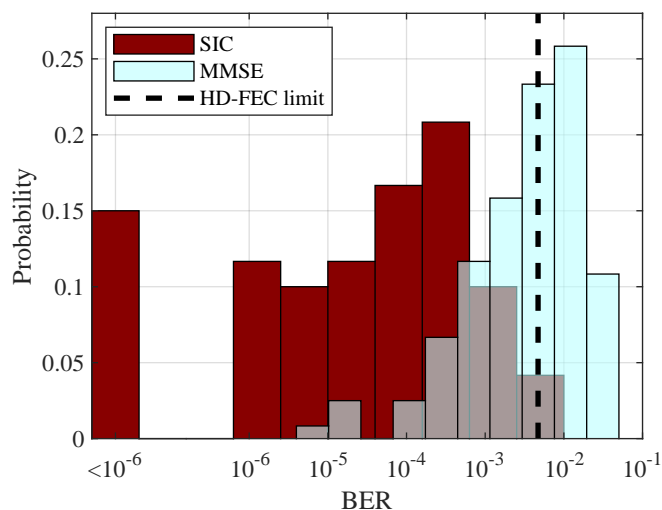
SIC system, while the implementation penalty of the MMSE system is ~8.2 dB. When compared with the corresponding results in Fig. 7, we can conclude that a significantly better turbulence and device imperfection resiliency can be obtained under different turbulence conditions by increasing the number of redundant receive channels in the MDM FSO system.

Fig. 13 depicts the BER performance of a 6×12 system using 120 independent patterns, which are the same as the patterns used in Fig. 10, under the stronger turbulence case without noise loading. Similar to Fig. 10, the BER of the SIC system is consistently lower than the MMSE system. As a result, the average BER among different turbulence realizations is decreased from 1.56×10^{-4} to 2.86×10^{-6}. If we consider an outage when the BER is larger than the HD-
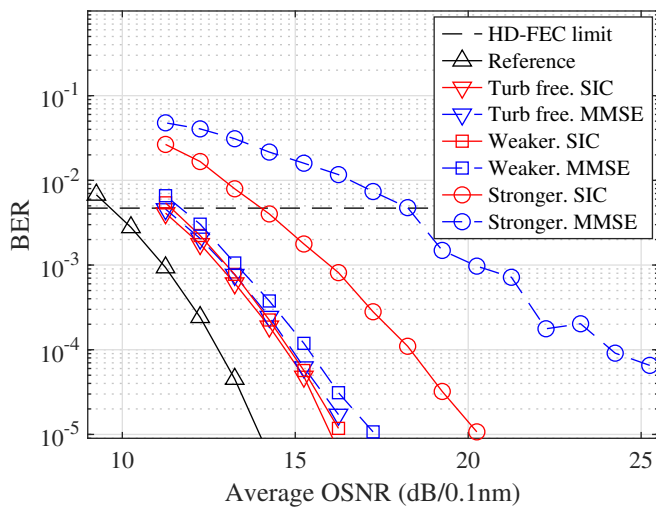
9

Fig. 12. Average BER curves of the 6×12 MIMO system under different turbulence intensities. Reference: Theoretical reference curve in an ideal system; Turb free: turbulence free system with a blank pattern. Weaker: typical weaker turbulence pattern when $r_0 = 3.0\,\mathrm{mm}$; Stronger: typical stronger turbulence pattern when $r_0 = 0.8\,\mathrm{mm}$.
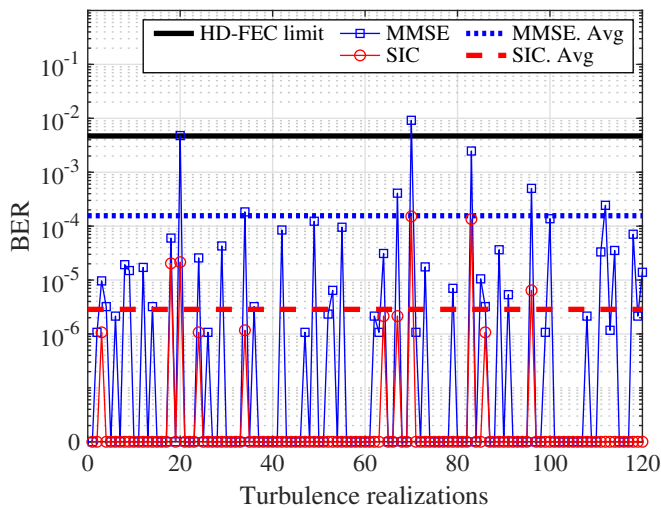

Fig. 13. The BER performance of the 6×12 MIMO system under 120 stronger turbulence realizations.

FEC limit, the outage probability of the MMSE and the SIC system will be decreased to 1.67% and 0%, respectively. When compared with the corresponding results in Fig. 10, we can conclude that a significantly better turbulence resiliency can be obtained in different turbulence realizations by increasing the number of redundant receive channels.

In order to comprehensively compare different transmit and receive channel numbers as well as different MIMO decoding algorithms, Fig. 14 depicts the average BER performance of different MIMO systems using 120 independent patterns under the strong turbulence case without noise loading. As shown in Fig. 14, when the number of transmit channels (N_t) is fixed, the average BER will decrease as the number of receive channels (N_r) increases. On the other hand, when N_r is fixed, the average BER will increase as N_t increases. Moreover, in the same system setup when N_t and N_r are both fixed, the SIC
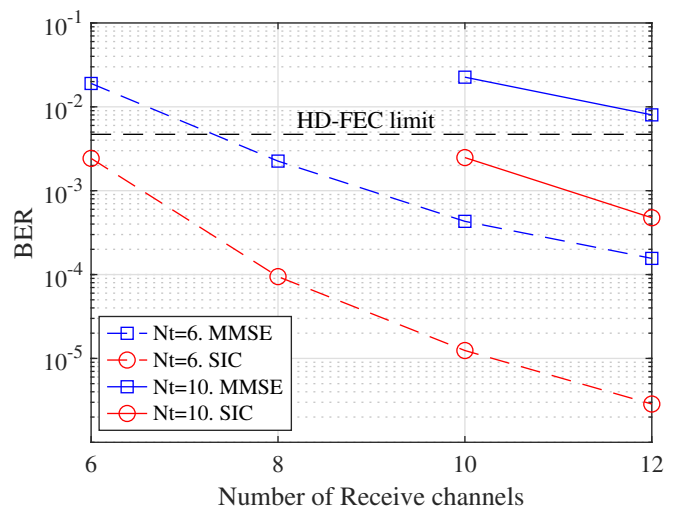

Fig. 14. The average BER performance of different MIMO systems under 120 stronger turbulence realizations.

algorithm always performs better than the MMSE algorithm.

VI. CONCLUSION

In this paper, we experimentally demonstrate the enhanced turbulence resiliency in a MDM FSO communication link with 5 transmitted spatial modes, each carrying a 34.46 GBaud DP-QPSK signal. By employing the SIC MIMO algorithm and redundant receive channels, the average BER of the 10×12 MIMO system goes down to 4.76×10^{-4}, which is well below the HD-FEC limit, among 120 independent turbulence realizations where $D = 8.4\,\mathrm{mm}$ and $r_0 = 0.8\,\mathrm{mm}$ ($D/r_0 = 10.5$). Moreover, the outage probability is significantly decreased when using the SIC algorithm, which indicates the possibility of a much more robust transmission in the MDM FSO system through turbulent channels.

We also compare the system performance among systems with different transmit and receive channel numbers. The results indicate that we can obtain an even better BER performance by increasing the number of redundant receive channels. These results may also provide useful guidelines when deploying the MDM FSO system in an even stronger turbulence environment.

As a result, the system demonstrates a record-high independent channel number of 10 and line rate of 689.23 Gbit/s. Considering the 8.4% training sequence, 10% pilot rate, 6.25% HD-FEC cost, and 0.1 rolloff factor, a record-high net spectral efficiency of 13.9 bit/s/Hz was also achieved in emulated turbulent MDM FSO links.

REFERENCES

[1] Y. Ren, Z. Wang, P. Liao, L. Li, G. Xie, H. Huang, Z. Zhao, Y. Yan, N. Ahmed, A. Willner *et al.*, "Experimental characterization of a 400 Gbit/s orbital angular momentum multiplexed free-space optical link over 120 m," *Optics letters*, vol. 41, no. 3, pp. 622–625, 2016.

[2] R. Lange, B. Smutny, B. Wandernoth, R. Czichy, and D. Giggenbach, "142 km, 5.625 Gbps free-space optical link based on homodyne BPSK modulation," in *Free-space laser communication technologies XVIII*, vol. 6105. International Society for Optics and Photonics, 2006, p. 61050A.

[3] M. A. Khalighi and M. Uysal, "Survey on free space optical communication: A communication theory perspective," *IEEE communications surveys & tutorials*, vol. 16, no. 4, pp. 2231–2258, 2014.

[4] J. Wang, J.-Y. Yang, I. M. Fazal, N. Ahmed, Y. Yan, H. Huang, Y. Ren, Y. Yue, S. Dolinar, M. Tur *et al.*, "Terabit free-space data transmission employing orbital angular momentum multiplexing," *Nature photonics*, vol. 6, no. 7, pp. 488–496, 2012.

[5] N. K. Fontaine, R. Ryf, Y. Zhang, J. C. Alvarado-Zacarias, S. van der Heide, M. Mazur, H. Huang, H. Chen, R. Amezcua-Correa, G. Li, M. Capuzzo, R. Kopf, A. Tate, H. Safar, C. Bolle, D. T. Neilson, E. Burrows, K. Kim, M. Bigot-Astruc, F. Achten, P. Sillard, A. Amezcua-Correa, and J. Carpenter, "Digital turbulence compensation of free space optical link with multimode optical amplifier," in *45th European Conference on Optical Communication (ECOC 2019)*, 2019, pp. 1–4.

[6] A. E. Willner, Z. Zhao, C. Liu, R. Zhang, H. Song, K. Pang, K. Manukyan, H. Song, X. Su, G. Xie *et al.*, "Perspectives on advances in high-capacity, free-space communications using multiplexing of orbital-angular-momentum beams," *Apl Photonics*, vol. 6, no. 3, p. 030901, 2021.

[7] Z. Qu and I. B. Djordjevic, "500 Gb/s free-space optical transmission over strong atmospheric turbulence channels," *Optics Letters*, vol. 41, no. 14, pp. 3285–3288, 2016.

[8] Y. Ren, G. Xie, H. Huang, N. Ahmed, Y. Yan, L. Li, C. Bao, M. P. Lavery, M. Tur, M. A. Neifeld *et al.*, "Adaptive-optics-based simultaneous pre-and post-turbulence compensation of multiple orbital-angular-momentum beams in a bidirectional free-space optical link," *Optica*, vol. 1, no. 6, pp. 376–382, 2014.

[9] A. Trichili, K.-H. Park, M. Zghal, B. S. Ooi, and M.-S. Alouini, "Communicating using spatial mode multiplexing: Potentials, challenges, and perspectives," *IEEE Communications Surveys & Tutorials*, vol. 21, no. 4, pp. 3175–3203, 2019.

[10] R. Brüning, Y. Zhang, M. McLaren, M. Duparré, and A. Forbes, "Overlap relation between free-space Laguerre Gaussian modes and step-index fiber modes," *JOSA A*, vol. 32, no. 9, pp. 1678–1682, 2015.

[11] L. C. Andrews and R. L. Phillips, *Laser Beam Propagation through Random Media, Second Edition*. SPIE Press, 2005.

[12] M. P. Lavery, "Vortex instability in turbulent free-space propagation," *New Journal of Physics*, vol. 20, no. 4, p. 043023, 2018.

[13] L. Li, R. Zhang, P. Liao, Y. Cao, H. Song, Y. Zhao, J. Du, Z. Zhao, C. Liu, K. Pang *et al.*, "Mitigation for turbulence effects in a 40-Gbit/s orbital-angular-momentum-multiplexed free-space optical link between a ground station and a retro-reflecting UAV using MIMO equalization," *Optics letters*, vol. 44, no. 21, pp. 5181–5184, 2019.

[14] M. A. Cox, L. Maqondo, R. Kara, G. Milione, L. Cheng, and A. Forbes, "The resilience of Hermite–and Laguerre–Gaussian modes in turbulence," *Journal of Lightwave Technology*, vol. 37, no. 16, pp. 3911–3917, 2019.

[15] S. Chen, S. Li, Y. Zhao, J. Liu, L. Zhu, A. Wang, J. Du, L. Shen, and J. Wang, "Demonstration of 20-Gbit/s high-speed Bessel beam encoding/decoding link with adaptive turbulence compensation," *Optics letters*, vol. 41, no. 20, pp. 4680–4683, 2016.

[16] T. Weyrauch, M. A. Vorontsov, T. G. Bifano, J. A. Hammer, M. Cohen, and G. Cauwenberghs, "Microscale adaptive optics: wave-front control with a μ-mirror array and a VLSI stochastic gradient descent controller," *Applied Optics*, vol. 40, no. 24, pp. 4243–4253, 2001.

[17] S. W. Paine and J. R. Fienup, "Machine learning for improved image-based wavefront sensing," *Optics letters*, vol. 43, no. 6, pp. 1235–1238, 2018.

[18] Y. Nishizaki, M. Valdivia, R. Horisaki, K. Kitaguchi, M. Saito, J. Tanida, and E. Vera, "Deep learning wavefront sensing," *Optics express*, vol. 27, no. 1, pp. 240–251, 2019.

[19] S. Yang and X. Li, "Derivation of ambiguity in wavefront aberration and quantitative analysis in AO system," *Optics and Lasers in Engineering*, vol. 158, p. 107174, 2022.

[20] H. Huang, Y. Cao, G. Xie, Y. Ren, Y. Yan, C. Bao, N. Ahmed, M. A. Neifeld, S. J. Dolinar, and A. E. Willner, "Crosstalk mitigation in a free-space orbital angular momentum multiplexed communication link using 4×4 MIMO equalization," *Optics letters*, vol. 39, no. 15, pp. 4360–4363, 2014.

[21] Y. Ren, Z. Wang, G. Xie, L. Li, A. J. Willner, Y. Cao, Z. Zhao, Y. Yan, N. Ahmed, N. Ashrafi *et al.*, "Atmospheric turbulence mitigation in an OAM-based MIMO free-space optical link using spatial diversity combined with MIMO equalization," *Optics letters*, vol. 41, no. 11, pp. 2406–2409, 2016.

[22] R. G. Van Uden, C. M. Okonkwo, H. Chen, H. de Waardt, and A. M. Koonen, "Time domain multiplexed spatial division multiplexing receiver," *Optics express*, vol. 22, no. 10, pp. 12 668–12 677, 2014.

[23] G. Rademacher, B. J. Puttnam, R. S. Luís, T. A. Eriksson, N. K. Fontaine, M. Mazur, H. Chen, R. Ryf, D. T. Neilson, P. Sillard *et al.*, "Peta-bit-per-second optical communications system using a standard cladding diameter 15-mode fiber," *Nature Communications*, vol. 12, no. 1, pp. 1–7, 2021.

[24] K. Shibahara, T. Mizuno, and Y. Miyamoto, "MIMO carrier phase recovery for carrier-asynchronous SDM-MIMO reception based on the extended Kalman filter," *Optics Express*, vol. 29, no. 11, pp. 17 111–17 124, 2021.

[25] J. G. Proakis and M. Salehi, *Digital communications*. McGraw-hill New York, 2001, vol. 4.

[26] D. Tse and P. Viswanath, *Fundamentals of wireless communication*. Cambridge university press, 2005.

[27] A. Zanella, M. Chiani, and M. Z. Win, "MMSE reception and successive interference cancellation for MIMO systems with high spectral efficiency," *IEEE Transactions on wireless Communications*, vol. 4, no. 3, pp. 1244–1253, 2005.

[28] J. Benesty, Y. Huang, and J. Chen, "A fast recursive algorithm for optimum sequential signal detection in a BLAST system," *IEEE Transactions on Signal Processing*, vol. 51, no. 7, pp. 1722–1730, 2003.

[29] S. Saito, H. Suganuma, K. Ogawa, and F. Maehara, "Performance enhancement of OAM-MIMO using successive interference cancellation," in *2019 IEEE 89th Vehicular Technology Conference (VTC2019-Spring)*. IEEE, 2019, pp. 1–5.

[30] A. Jaiswal and M. R. Bhatnagar, "Free-space optical communication: A diversity-multiplexing tradeoff perspective," *IEEE Transactions on Information Theory*, vol. 65, no. 2, pp. 1113–1125, 2018.

[31] Y. Li, C. Gao, M. S. Leeson, and X. Li, "Asymptotic analysis of V-BLAST MIMO for coherent optical wireless communications in Gamma-Gamma turbulence," *Optics Express*, vol. 26, no. 21, pp. 27 931–27 944, 2018.

[32] Y. Li, Z. Hu, D. M. Benton, A. Ali, M. Patel, and A. D. Ellis, "Demonstration of 10-channel mode-and polarization-division multiplexed free-space optical transmission with successive interference cancellation DSP," *Optics Letters*, vol. 47, no. 11, pp. 2742–2745, 2022.

[33] Z. Hu, Y. Li, D. M. Benton, A. A. Ali, M. Patel, and A. D. Ellis, "Single-wavelength transmission at 1.1-Tbit/s net data rate over a multimodal free-space optical link using commercial devices," *Optics Letters*, vol. 47, no. 14, pp. 3495–3498, 2022.

[34] R. G. Lane, A. Glindemann, and J. C. Dainty, "Simulation of a Kolmogorov phase screen," *Waves in Random Media*, 1992.

[35] M. Chen and M. Lavery, "Optical angular momentum interaction with turbulent and scattering media," in *Structured Light for Optical Communication*. Elsevier, 2021, pp. 237–258.

[36] Y. Li, Z. Hu, and A. Ellis, "CRLB Approaching Pilot-aided Phase and Channel Estimation Algorithm in MIMO Systems with Phase Noise and Quasi-Static Channel Fading," *arXiv preprint arXiv:2112.02583*, 2021.

[37] R. G. van Uden, C. M. Okonkwo, V. A. Sleiffer, H. de Waardt, and A. M. Koonen, "MIMO equalization with adaptive step size for few-mode fiber transmission systems," *Optics express*, vol. 22, no. 1, pp. 119–126, 2014.

[38] L. M. Zhang and F. R. Kschischang, "Staircase codes with 6% to 33% overhead," *Journal of Lightwave Technology*, vol. 32, no. 10, pp. 1999–2002, 2014.